Towards the ultimate strength of iron: spalling through laser shock

Gaia Righi [a], Carlos J. Ruestes [b], Camelia V. Stan [c], Suzanne J. Ali [c], Robert E. Rudd [c], Megumi Kawasaki [d], Hye-Sook Park [c], Marc A Meyers [a],[*]

[a] *University of California, San Diego, La Jolla, CA 92093, USA*
[b] *Universidad Nacional de Cuyo, Padre J. Contreras 1300, 5500 Mendoza, Argentina*
[c] *Lawrence Livermore National Laboratory, Livermore, CA 94550, USA*
[d] *Oregon State University, Corvallis, OR 97331, USA*

ARTICLE INFO

ABSTRACT

The ultimate strength of materials is reached at strain rates approaching the Debye frequency, when the deformation time at the atomic scale approaches the time for atoms to move away from the equilibrium to their extreme separation position ($\sim 5.5 \times 10^{13}$ s^{-1} for iron). We conducted high-power pulsed laser experiments on single, poly-, and nanocrystalline iron, generating tensile pulses with strain rates approaching the Debye frequency, 10^6 s^{-1} – 10^7 s^{-1}, and nanosecond time durations. We find iron strengths varying between 5 and 10 GPa, a factor of ten higher than the static tensile strength. Ultrafine-grained iron samples exhibit a lower tensile strength, $\sim$4-6 GPa, than single crystal iron, $\sim$10 GPa. MD simulations show that this is due to differences in the initiation sites for voids, primarily at grain boundaries for the nano- and polycrystalline conditions. Sparse runaway voids ($\sim$5 μm diameter) and evidence of surface melting are observed for the single crystal iron and are likely due to strain-induced melting when sufficient deformation occurs. The process of separation leading to spalling is modeled by molecular dynamics, and the mechanisms observed in the experimentally recovered specimens are determined: in single crystals voids nucleate at the intersection of twins, while in nanocrystalline specimens grain boundaries are the principal sources of void nucleation. Analytical calculations are applied to the dislocations generated by the emission of shear loops from the void surfaces and the geometrically necessary dislocation densities are found to be consistent with predictions from molecular dynamics calculations.

© 2021

1. Introduction

Spalling plays an important role in high-velocity impact, for example in ballistics, geological events, and aerospace debris. Damaging spall can be caused by the impact of a projectile or debris onto a surface, or from ejection of material after the formation of an impact crater [1–3]. This is due to the interaction of stress waves during shock compression and release; spall fracture occurs due to the tensile stress generated by a reflecting shock at a material boundary [4,5]. The spall strength of materials under dynamic tensile loading conditions has been found to have a "reverse" Hall-Petch relationship, increasing with increasing grain size [6–9].

The spall strength of iron (Fe) is of interest to geophysics and structural engineering, as it is a major component of meteorites and rocky planetary cores, and of steels and alloys. Spallation in iron has been studied in the past with flyer plate and gas gun methods at strain rates up to 10^5 s^{-1} [6,10–12] and through molecular dynamics (MD) at strain rates above 10^9 s^{-1} [13–15], but little work has been done using lasers to spall iron [9,16–18]. Iron undergoes the α to ε phase transformation at $\sim$13 GPa during compression [19] and the reverse (upon unloading) at $\sim$10 GPa [20–22]. Laser shock-induced spall experiments in polycrystalline iron revealed that damage is strongly affected by the α to ε phase transformation; smooth spall and a dense twin distribution are the result of spall occurring after the reverse phase transformation upon unloading, similar to observations at lower strain rates [18–22]. Thin samples (250 μm) that were transformed to ε-Fe were found to have a smooth spall with dense twin distribution, while thicker samples (400 μm) that remained mostly in the α phase showed brittle spall and a lack of twins [18]. This was further investigated with MD simulations of nanocrystalline iron, where a phase-transforming potential shows that after the ε-α phase transformation there is a much higher density of twins and a smoother spall surface, while a phase-stable potential shows many cracks and rough spall [14]. The formation of a substructure and twin boundaries resulting from the phase transforma-

tion provides an increased concentration of void nucleation sites, eventually leading to ductile spall. Other laser shock-induced spall experiments show that single crystal iron has a higher spall strength and a ductile fracture surface while polycrystalline iron is softer and spalls along grain boundaries [9], and that spall strength increases with increasing strain rate [16,17].

Clearly, behavior of iron spallation changes as a function of applied high strain rate and initial microstructure, but there has never been a systematic study to understand the interdependence of these effects. In this work we aim to determine spall strength dependence on grain size (single, poly, and nanocrystalline) and strain rate (10^6 s^{-1} – 10^7 s^{-1}) in pure iron.

2. Experimental and Computational Methods

2.1. Materials

Iron samples consisted of single crystal iron foils of 250 μm (Accumet Materials Co, 99.94 + %) or 100 μm thickness (Surface Preparation Laboratory, ~99.98%), polycrystalline foils of 100 μm and 250 μm thickness (Goodfellow, ~99.5%), and nanocrystalline foils that were produced from 1 mm thick single crystal samples (Accumet Materials Co, 99.94 + %) using high-pressure torsion (HPT). The HPT process was conducted for 20 turns at 2 GPa to produce an average grain size of ~100 nm. All foils were then laser cut to 2.5 × 2.5 mm squares and mechanically polished to an optical finish using 30, 12, 9, and 5 μm silicon carbide and aluminum oxide paper, followed by 1 μm diamond suspension. Unshocked samples were further mechanically polished to 0.04 μm finish using a colloidal silica suspension. Final thicknesses are reported in Table 1.

Grain sizes were determined through Electron Backscatter Diffraction (EBSD) on a FEI Apreo Field Emission Scanning Electron Microscope (FESEM). EBSD confirmed that the single crystal had no grain boundaries and [001] was oriented in the shock direction. Grain sizes were found to be 100-250 μm elongated and 100 nm equiaxed to moderately elongated for poly- and nanocrystalline iron, respectively (Fig. 1).

2.2. Experimental Design

A 30 μm thick polystyrene (PS) ablator was adhered to one side of each sample foil using Hardman Double Bubble epoxy. All glue was tacked on the edges to minimize the gap between the
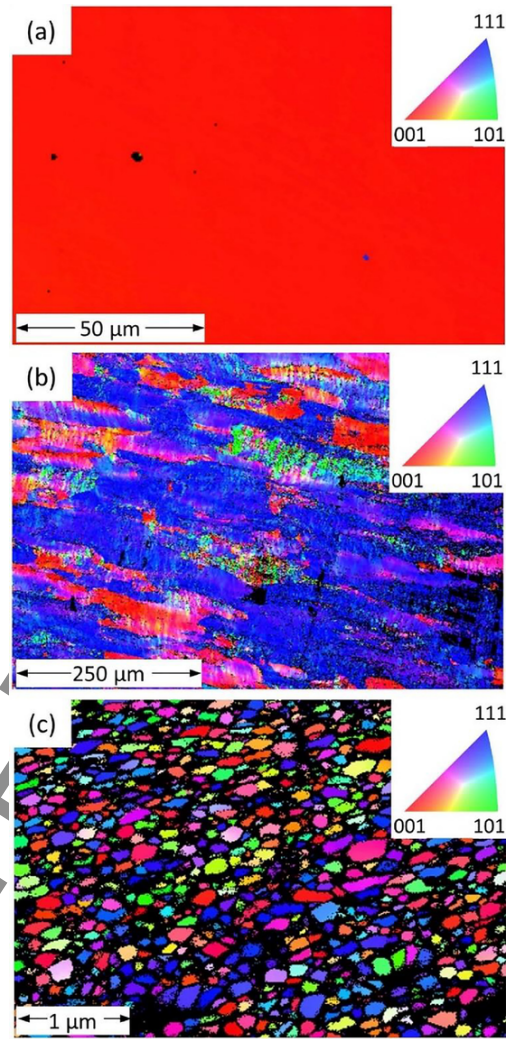

Figure 1. EBSD maps of (a) single crystal, (b) polycrystal, and (c) nanocrystal iron. The single crystal map shows no grain boundaries and strong [001] orientation where unindexed black spots are remnant polishing media. The polycrystal map shows grain sizes ranging from 100-250 μm with a slight preferred orientation of [111] where unindexed pixels are due to scratches. The nanocrystal map shows grain size averaging around 100 nm with no preferred orientation where unindexed pixels around grain boundaries are due to the high strain associated with HPT. Single and polycrystal maps taken with 0.5 μm step size and nanocrystal map taken with 10 nm step size.

sample surface and ablator. This assembly was then glued to a stainless-steel washer with 10 mm outer diameter and 2 mm inner diameter. Recovery gel (Gelly brand candle wax) was molten onto a debris shield, and upon solidifying was placed approximately 15 cm behind the target in the expected direction of motion (Fig. 2a).

Samples were laser shocked in Target Area 1 of the Jupiter Laser Facility at Lawrence Livermore National Laboratory. The 100 J 2ω laser had a nominal square pulse shape with 10 ns duration and 1 mm spot size, resulting in peak power of approximately 1 TW/cm^2. VISAR (velocity interferometry system for any reflector) [23,24] was used to record the velocity of the sample rear free surface (Fig. 2b) from which spall strength, peak pressure, and strain rates are calculated. Two independent interferometers were used to ensure the data is conclusive and appropriately calibrated (etalon thicknesses: d_1 = 49.968 mm and d_2 = 100.21 mm). 1-D radiation hydrodynamic simulations using

Table 1
Material Parameters and Experimental Results[*]

	Polished thickness (μm)	Peak pressure (GPa)	Strain rate (10^7 s^{-1})	Spall strength (GPa)
Single	100 (10)	81.78 (35)	2.33 (0.25)	10.69 (3.01)
	170 (20)	66.11 (10)	2.15 (0.63)	9.90 (1.00)
Poly	100 (10)	61.28 (29)	2.12 (1.52)	8.54 (1.32)
	250 (25)	62.49 (33)	0.36 (0.11)	4.32 (0.36)
Nano	100 (30)	106.4	2.46	6.60
	200 (30)	94.7	1.46	4.95

[*] Values in parentheses represent standard deviation due to variation in sample thickness.
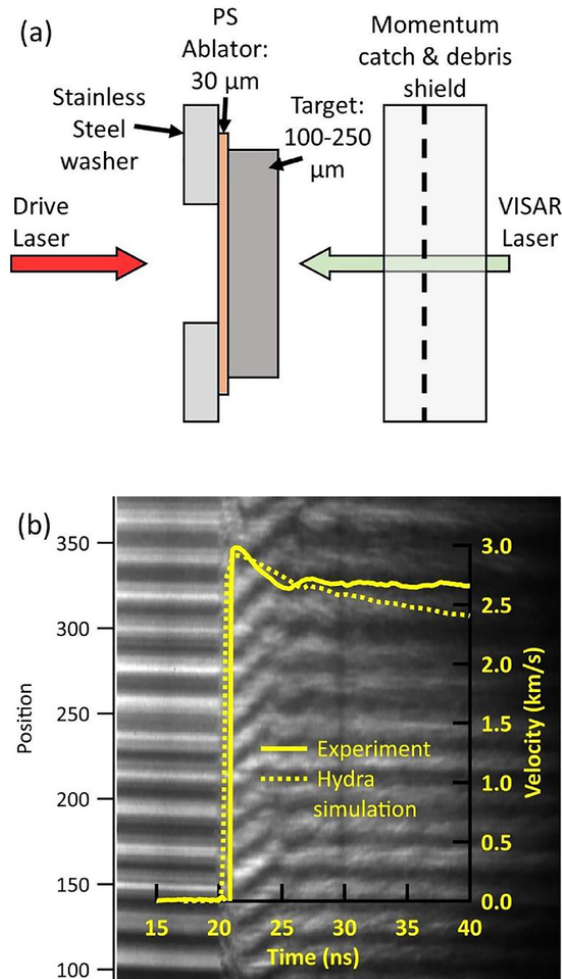
Figure 2. (a) Experimental set-up. The iron target is glued onto polystyrene ablator, which is then glued onto a stainless steel washer. Composite is placed in the target mount and the debris shield and momentum catch (polymer gel) is placed behind target. VISAR laser is simultaneously used with the drive laser to capture interference fringes from the free surface. (b) 1-D radiation-hydrodynamic simulations predict free surface velocity similar to experimental measurement.

HYDRA [25] were run to predict peak pressure and spall strength (Fig. 2b).

2.3. Computational Modelling

Non-equilibrium MD simulations of shock compression were performed, following widely used methods [14,26–30]. Experimental laser shock compression was modeled by introducing a time-dependent piston velocity profile which dictates the prescribed shock density and strain rate [26]. The controlled acceleration and deceleration profiles mimic the stress profile introduced during shock compression [14,27,31]. The piston was linearly accelerated to 800 m/s over 5 ps, maintained at that velocity for 20 ps, then decelerated to stationary over 20 ps. As a result, and by considering the strain rate to be approximated by the spatial derivative of the particle velocity, the longitudinal strain rate at the point of maximum tension is approximately 10^{10} s^{-1}. Although higher than the experimentally applied strain rates, it will be shown in Section 3.3 that it is adequate to capture the deformation mechanisms taking place in the experiments. Four Fe configurations were modeled, single crystal with [001] oriented in the shock direction, and three

nanocrystalline samples with average grain sizes of 14, 12, and 10 nm. The nanocrystalline samples were prepared using Atomsk [32] with sample dimensions of $50 \times 50 \times 150$ nm^3, comprising approximately 32 million atoms. Periodic boundary conditions transverse to the shock direction (z) were employed, allowing for unconstrained expansion of the free surface in the shock direction. An Embedded Atom Model (EAM) potential was fit to adequately reproduce the α-ε phase transition of Fe [14,28–30,33–36]. Simulations were run using LAMMPS [37] and visualization was performed using OVITO [38] post-processing algorithms (adaptive common neighbor analysis [39], polyhedral template matching [40], construct surface mesh [41] and dislocation extraction algorithm (DXA) [42]). The nanocrystalline samples were minimized and thermally annealed at $0.7T_{melt}$ for 0.5 ns. All samples were thermalized at 300 K and zero pressure prior to loading.

In addition to non-equilibrium MD, a nanometer-sized void in iron was modeled using the same potential as described above. The simulation domain was initially set up as a cubic single crystal sample containing 56^3 unit cells with one spherical void (r = 1.5 nm) at the center of the sample. Periodic boundary conditions were imposed in all directions and the sample was equilibrated to zero pressure at an initial temperature of 300 K. A uniaxial tensile strain rate of 10^9 s^{-1} was applied in the [001] direction for 120 ps, resulting in a total of 12% volume strain with lateral strains impeded. A 1 fs time step was chosen, and the simulation was run with a constant NVE (number, volume, energy) integration consistent with the micro-canonical ensemble such that no temperature control is imposed, and temperature effects due to plasticity could be measured. DXA was used to identify line defects.

3. Results and Discussion

3.1. Microstructural characterization

Fractured surfaces can be described as either ductile or brittle depending on the mechanisms that occur during spallation. Ductile fracture is characterized by dimpled surface morphology that is the result of the nucleation, growth, and coalescence of voids, producing a continuous fracture surface. In contrast, brittle fracture is characterized by smooth facets that are the result of the separation of atomic bonds along specific crystallographic planes. The spalled surface of recovered samples was characterized by SEM, and EBSD was used to characterize cross-sections to understand the failure mechanism. Shocked single crystal iron (Fig. 3a, d, e) shows dimpling at the nanometer scale that is characteristic of ductile failure, while poly- and nanocrystal iron samples (Fig. 3b-c) show flaking that could be a result of failure via separation along grain boundaries (Fig. 3e). The high-pressure torsion process used to fabricate the nanocrystal samples produces thin, elongated grains along which the spall occurs. Evidence of these elongated grains can be seen in Fig. 3f. The dimple size in single and polycrystalline samples and the shear-like bands in nanocrystalline samples are on the order of 1 nm (Fig. 3g-i). In single crystal samples, a remnant of the spall plane can be seen near the edge of the sample (Fig. 4a), in which twin boundaries can be found (Fig. 4b). The unmapped region around the twin boundaries can be attributed to voids/cracks or possibly a highly strained region that EBSD is unable to map. The misorientation angle for the boundaries seen in Fig. 4b was measured to be ~60°, suggesting the formation of {001}/{112} twins. Additionally, these are found to be Σ3 boundaries (Fig. S1), which are known to result from twinning [43]. Randomly
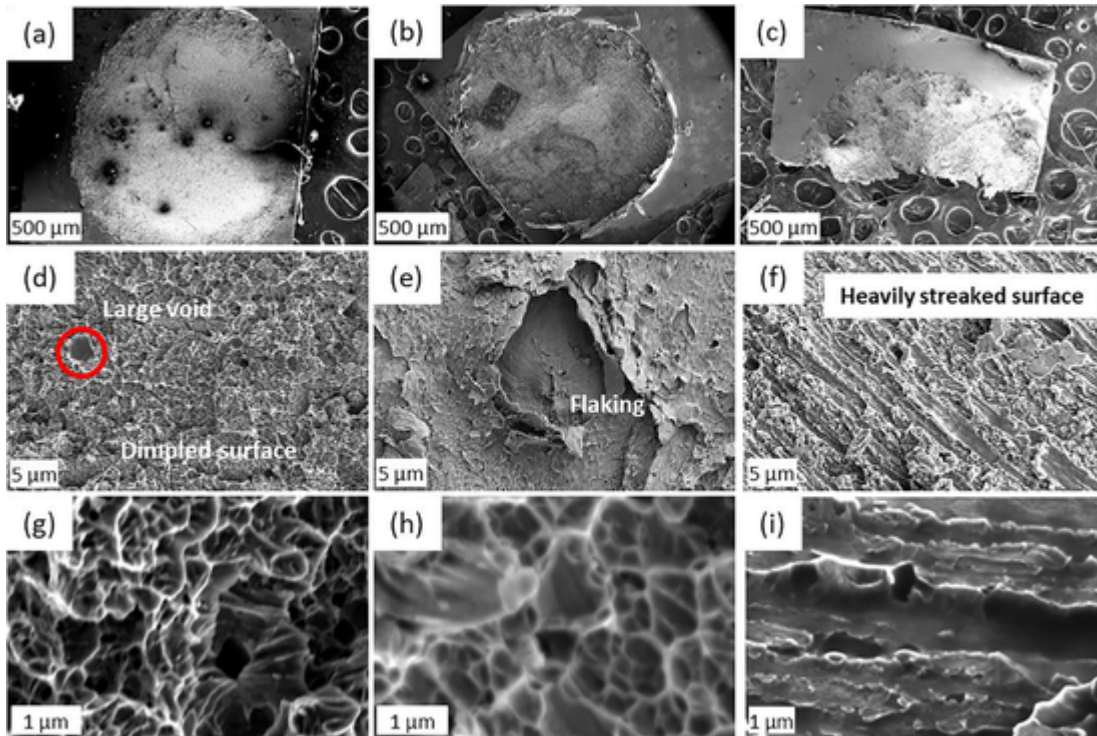
Figure 3. SEM images of single crystal (left), polycrystal (middle), and nanocrystal (right) at low (a-c), medium (d-f), and high (g-i) magnification. Dimpling in single and polycrystal iron is evidence of ductile fracture while shear-like bands in nanocrystal are evidence of spalling along grain boundaries. Dimple size in (g) and (h) and streak features in (i) are at the same length scale.

distributed voids are also seen through the cross section of the sample (Fig. 4c). For polycrystalline Fe, multiple spall layers can be seen in cross-sectional SEM images (Fig. 5a) with separation occurring along grain boundaries where there is a large density of voids (Fig. 5b).

The density of geometrically necessary dislocations (GNDs) was mapped using Matlab toolbox MTEX according to the method of Pantleon [44]. In both cases, GND density is approximately 10^{15} m^{-2} (Figs. 4d-e, 5d-e), which is consistent with heavily work-hardened metals [43] as well as shock compressed tantalum [45,46]. Furthermore, this technique underestimates the GND density as 3D maps are needed for a more accurate measurement. The circular regions with high dislocation densities (Fig. 4e) are due to sub-surface voids that emit shear dislocation loops (Fig. 4f). When these loops intersect the polished surface, they generate the circular regions of high GND density. These are evidence for the shear loop emission mechanisms for void growth described in Section 3.4. Evidence of intragranular plasticity can be seen in the polycrystalline samples (Fig. 5d-e) where there is higher GND density within grains. This observation is also evident in simulations as described in Section 3.3.

Vestiges of a brittle fracture mechanism were observed at the edges of the spall plane (Fig. 6), where pressure and strain rate are lower than at the center of the sample. This can be explained by a brittle-to-ductile spall transition occurring at a critical strain rate, as described by Grady [47]. For iron, this critical strain rate is calculated to be on the order of 10^5 s^{-1}, a reasonable value for the edge of the spalled region where the shock has decayed. Smaller grained samples, however, do not display this behavior near the spall edge, because their spall behavior is dominated by grain boundaries. This shift in spall morphology is consistent with previous observations summarized by Meyers and Aimone [48].

Voids ($\sim$10 μm diameter) on the spalled surface were seen exclusively in single crystal samples (Fig. 7), with smooth inner surfaces which are indicative of melting and re-solidification of the material. During shock compression the temperature is expected to rise [4], but not enough to melt the entire sample. Section 3.3 will discuss molecular dynamic calculations that determine the temperature both of the overall sample and locally around a void.

The formation of voids can occur through a variety of mechanisms operating at different length scales (Fig. 8) [49–53]. At the atomic scale, intrinsic vacancy complexes can form nanoscale voids [50], although larger scale defects would dominate over such small-scale imperfections. Deformation-induced dislocation cell walls with a critical misorientation have large strain energy that can be relieved through void nucleation [54,55]. At larger length scales twin and grain boundaries are common void initiation sites (Section 3.3), because their high interfacial energy and weak bonding allow for the preferential nucleation of voids [51,52]. Second-phase particles or inclusions can cause cracks to propagate into the matrix material, which in turn can cause debonding of interfaces [49].

3.2. Spall strength determination

The experimental strain rate and spall strength were calculated from the free surface velocity profiles using the peak free surface velocity, u_{max}, and first minimum free surface velocity, u_{min} (also known as the spall pullback signal). The simplified acoustic approach yields the following linear approximation relationship between spall strength and the particle velocity drop (u_{max}-u_{min}) [5]:

$$P_{spall} = (1/2)\,\rho_0 c \left(u_{max} - u_{min} \right) \tag{1}$$
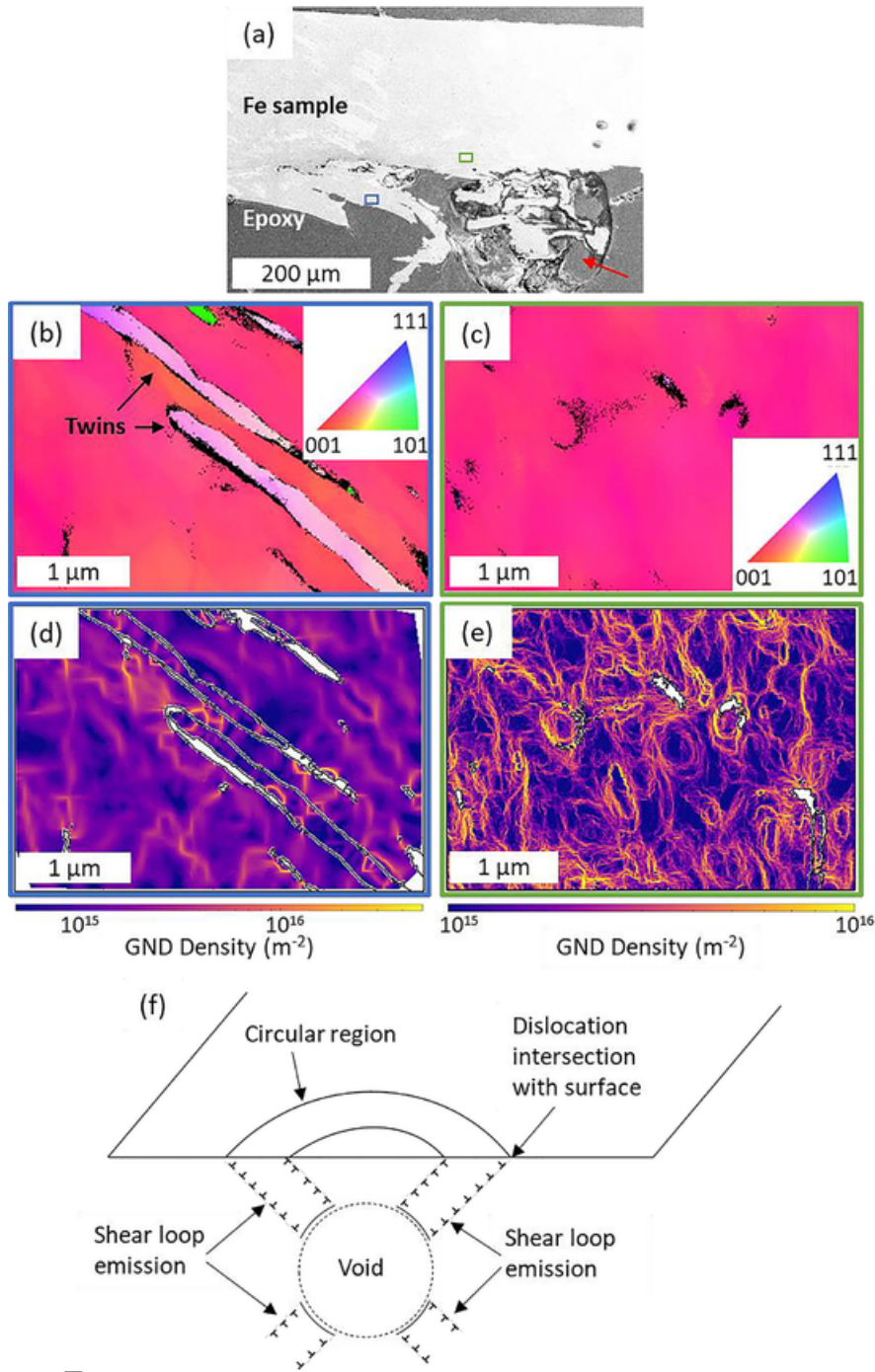
Figure 4. (a) Cross-section SEM image of shocked single crystal iron. Red arrow points to epoxy bubble. (b) EBSD mapping (IPF Z) near the spall plane shows large concentration of voids in vicinity of the twin boundary and (c) EBSD mapping further from the spall plane shows randomly spaced void groups. (d-e) Density of geometrically necessary dislocations is plotted for each EBSD map showing concentrations around 10^{15} m^{-2} in the bulk material and regions of higher concentration around twins or voids. (f) Void in the sub-surface emitting dislocations and producing circular features as seen in (e).

where ρ_0 is the initial density and c is the sound velocity of iron [4]. The strain rates were calculated by applying the following acoustic approximation:

$$\dot{\epsilon} = \frac{(u_{max} - u_{min})}{\Delta t \times 2c} \qquad (2)$$

where Δt is the time difference between u_{max} and u_{min}. The approximate strain rate for the 250 μm thick samples was $\sim 10^6$ s^{-1}, and a reduction in thickness to 100 μm increased the strain rate ten-fold, to $\sim 10^7$ s^{-1}. The peak pressure achieved during the spallation event was calculated using the Hugoniot relationship between pressure and particle velocity, assuming particle velocity is approximately half of the free surface velocity. Peak pressures ranged from 60 GPa – 100 GPa, well above the theoretical 13 GPa α-ε phase transformation pressure. Representative VISAR traces of free surface velocity depicting strain rate and grain size dependence can be seen in Fig. 9. The resulting strain rate and spall strengths for 50 shots are summarized in Table 1.

Figure 5. (a) Cross-section SEM image of shocked polycrystalline iron. (b) EBSD mapping (IPF Z) near the spall plane shows showing various cracks that are opening along grain boundaries and (c) EBSD mapping further from the spall plane. (d-e) Density of geometrically necessary dislocations is plotted for each EBSD map showing concentrations around 10^{15} m^{-2} in the bulk material and regions of higher concentration around sub-grain boundaries.
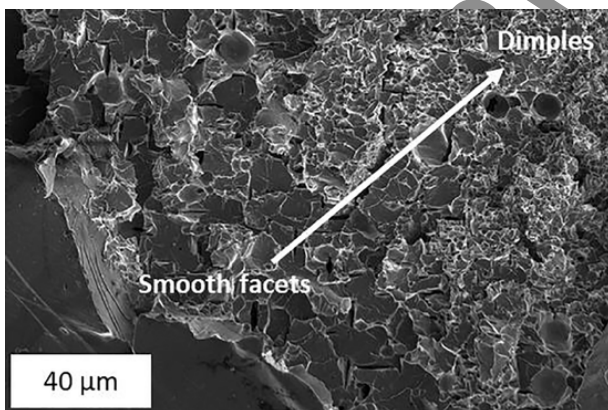

Figure 6. Single crystal iron spalled at 10^7 s^{-1} strain rate showing a transition from brittle failure at the spall edge to ductile failure near the sample center.

The spall strength is expected to be highest in single crystal because of the scarcity of fracture nucleation sites. Grain boundaries are a common nucleation site for voids under dynamic tensile loading, and for dislocation pile-up locations under shear loading [56]. The tensile strength of iron by slip is highly strain-rate dependent; in contrast, the strength of the grain boundaries can be considered to be strain-rate insensitive, to a first approximation. Thus, a critical strain rate is reached beyond which the slip stress is higher than the grain-boundary cohesion. At this strain rate, the failure mechanism changes from intragranular to intergranular failure. This result is in agreement with literature and spall theory that dates back three decades [5,9–11,13–18,47,56,57] (Fig. 10). The single crystal samples consistently show the highest spall strength, whereas the nanocrystalline samples have the lowest. Polycrystalline samples show much larger variation in spall strength, due to several factors: (1) large variation in grain size (5 – 250 μm), (2) sample purity (99.5 – 99.999%), and (3) sample processing conditions. Grain size, which is frequently unreported in the literature, will clearly affect spall strength, as smaller grains will have a larger grain boundary area per unit volume and therefore be weaker. Sample purity will also affect the spall strength as solute atoms tend to migrate towards grain boundaries to decrease strain energy. Lower purity iron will have more grain-boundary solutes which, in turn, decrease the grain boundary coalescence strength and
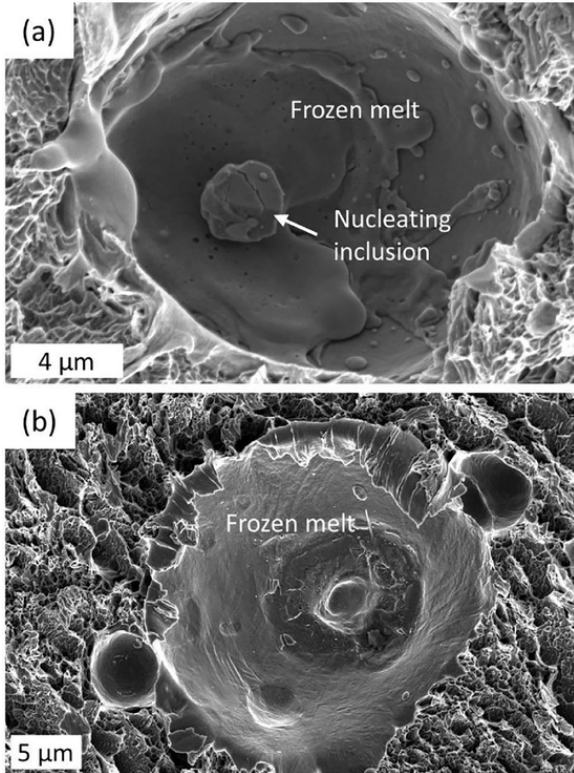
Figure 7. SEM images of voids found in single crystal iron. Voids are roughly 10 μm in diameter in both (a) high and (b) low strain rate samples. Smooth inner walls show evidence of melting inside the voids.

stress for nucleating voids. Differences in processing methods used in sample preparation can also introduce variations in the levels of strain in the structure. We fit the spall strengths by using power laws (Fig. 10), which converge at a high strain rate close to the Debye frequency, or the frequency of atomic vibrations. At this extreme strain rate the spall strength can be considered the ultimate tensile strength, 35 GPa [47], at which point the interatomic forces can no longer hold the structure together. The fit for polycrystalline iron does not currently converge because of the lack of experiments or simulations at strain rates higher than $\sim 10^8$ s^{-1} and inconsistencies in the grain structure. Similar failure behavior has been seen in spalled tantalum [7], vanadium [8], and iron at lower strain rate [18].

3.3. Molecular Dynamics Simulation of Spalling

As the initial shock runs across the sample, an α to ε phase transition takes place. This is expected after the results by Gunkelmann et al. [34] and Amadou et al. [28] for similar shock conditions. For the single crystal, the MD simulations reveal the nucleation of an ε phase that propagates along the sample in the shock direction, whereas for the nanocrystalline sample, the α to ε phase transition takes place within each grain, preserving the initial grain boundary structure. At later time, as the shock profile reflects from the rear surface of the sample, the reverse transition (ε to α) takes place. Similar conclusions were obtained in previous MD studies of uniaxial compression and release of polycrystalline iron [33]. These processes take place before any spallation event.

Stress profiles in iron samples were calculated from non-equilibrium MD simulations along the shock direction for dif-

ferent times around the beginning of spallation (Fig. 11). Positive values of σ_{zz} indicate tension. Assuming that the spall strength is equal to the peak tensile stress along the shock direction, the single crystal strength is 18 GPa, while the nanocrystal strength is 14.5 GPa. There was no significant strength variation with grain size for the nanocrystalline systems modeled here. The peak stress for the single crystal occurs in a region between 75 and 100 nm at about 56 ps, with a marked drop in stress 2 ps later. This drop signals the inception of the spallation event, with the formation of one or more closely spaced voids in that region. The stress peak is broader for the nanocrystalline sample, resembling a plateau that spans around 50 - 100 nm. In this instance, as time evolves (≥ 54 ps) stress drops occur in several positions along the plateau, signaling a distribution of the spallation event as voids open at several locations in this region. The delocalized spallation is due to the distributed nature of grain boundaries along the sample, two-dimensional defects that possess less strength and more void nucleation sites than in the single crystal.

In the single crystal samples, as voids nucleate due to twin-twin interactions and grow, they start coalescing, forming larger flaws, weakening the sample's section, and ultimately leading to the formation of a spallation plane (Fig. 12a). For the nanocrystalline simulations, however, the high fraction of grain boundaries offers energetically favorable nucleation sites for the formation of voids (Fig. 12b). The orientation of a grain boundary with respect to the wave propagation direction is more important than specific grain boundary orientation. This preferential failure along grain boundaries that are perpendicular to the loading direction is in agreement with previous studies on BCC metals [58]. Consequently, twinning is less pronounced, but can still be found in relatively large grains. In addition to experimental (Fig. 5d-e) and computational evidence (Fig. S2) of intragranular plasticity under spall conditions, similar observations can be found in the atomistic simulation literature: Gunkelmann and co-workers report intragranular plasticity in α-Fe for their nanocrystalline studies both under homogeneous compression [36] and under non-equilibrium shock compression [29]. Experimental evidence of intragranular plasticity is also found in both BCC and FCC metals [59–61]. Grain-boundary plasticity is another factor that can play an important role, particularly for grain sizes as small as the ones used in this work and under the high stresses induced by shock loading. To add complexity, grain boundary plasticity can also be rate dependent, as shown by grain-boundary disconnection motion studies [62]. Grain-boundary sliding and intragranular plasticity were identified in our simulations and can be seen in Fig. S2.

The time-resolved evolution of void nucleation and growth during spall in the [001]-oriented single crystal sample can be seen in Fig. 13. The polyhedral template matching algorithm was used to classify the local structural environment of the atoms. Twins (orange domains) nucleated during spall form elongated structures that, upon intersecting, favor the nucleation and growth of voids (Fig. 13). Void formation by twin-twin interaction was also reported by Gunkelmann et al [14] in Fe spall simulations and by Hahn et al. [27] in Ta spall simulations.

Temperature analysis around a void was performed following the discovery of regions that had the appearance of molten and resolidified material on the spalled surface of single crystal iron in experiments. Temperature was determined by:

$$T = \frac{1}{N} \sum_{n=1}^{N} \frac{m}{3k_b N_A} \left[v_{n,x}^2 + v_{n,y}^2 + \left(v_{n,z} - v_{CM,z} \right)^2 \right] \tag{3}$$
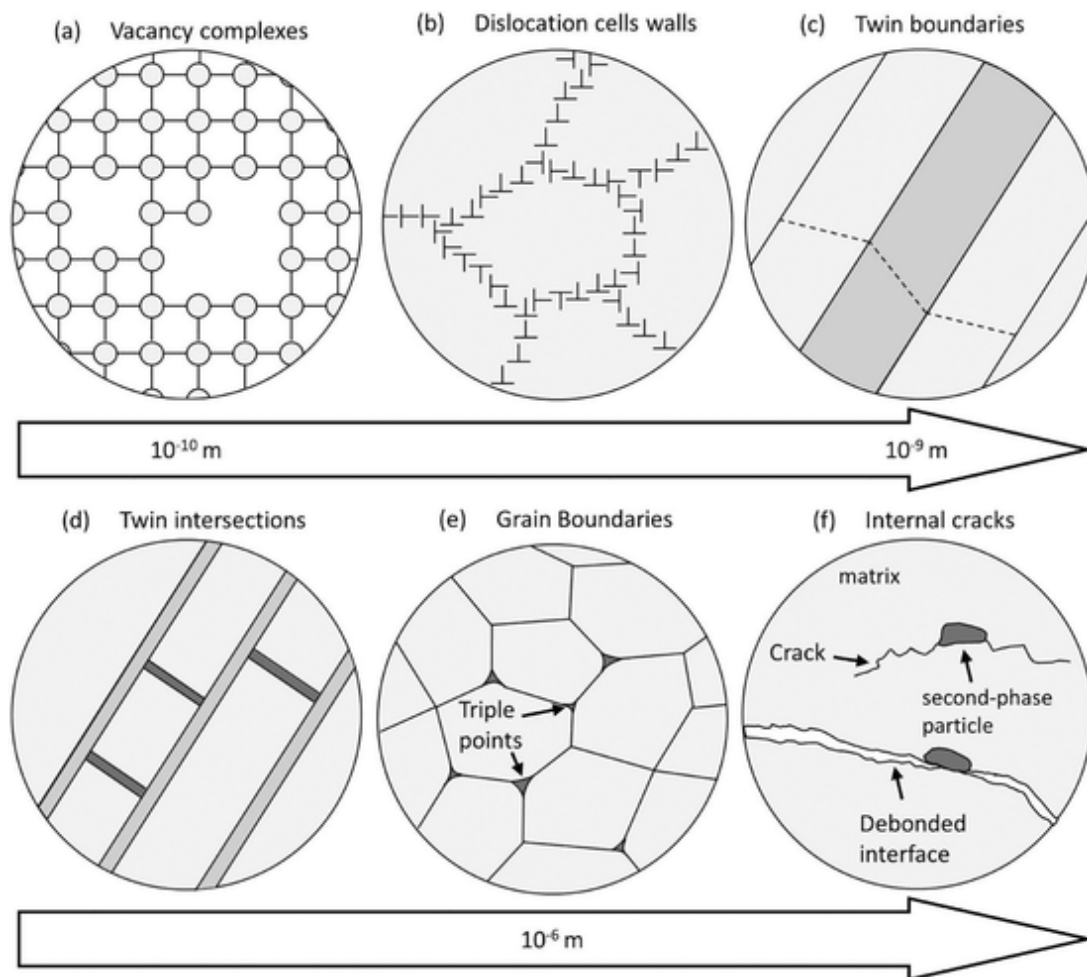
Figure 8. Hierarchy of void initiation sites. (a) vacancy complexes such as di- and tri-vacancies within the lattice [50], (b) dislocation cell walls [55], (c) twin boundaries with misorientation in the lattice, (d) twin interactions between primary and secondary twins, (e) grain boundaries [51] and triple points [49], (g) internal cracks and interface debonding at second-phase particles [49].

where the atomic mass of iron m is equal to 55.85 u, k_b is Boltzmann's constant, N_A is Avogadro's number, $v_{n,x}$, $v_{n,y}$, and $v_{n,z}$ are the components of the atom velocity vector, and $v_{CM,z}$ is the local center of mass translational velocity. Temperature profiles calculated from Eq. 3 for the single crystal and nanocrystalline sample during the time of the spallation process show that temperature is notably higher in the vicinity of the spallation plane (Fig. 11). The global temperature of the sample during spall was calculated to be 1000 K at most. However, due to the geometrically-necessary plastic deformation around voids, the temperature is increased locally (Fig. 11), approaching the decreased melting point caused by the tensile state during spall that relaxes the high pressure conditions [63]. This is indicated by the isolated data points (with error bars) in the region of the spall at 90 nm (and 60 ps) for the single crystal and by the three points between 60 and 100 nm for the nanocrystalline material. The spall region is more localized for the single crystal; the nanocrystalline sample provides ample regions for void initiation and therefore the spall region is more diffuse. As explained above, tensile stresses induce the formation of voids and temperature calculations around the voids reveal even higher temperatures, close to or above melting point.

3.4. Analytical model for dislocation generation around void surface

The MD predictions of high dislocation densities and temperatures around voids and the experimental observation of the apparent melting behavior stimulated the development of an analytical model for void-generating dislocations that increase the temperature. A nanometer-sized void is considered to act as a nucleation site for GNDs that, upon propagation away from the void, lead to successive nucleation and propagation events (Fig. 14). This yields a quantifiable dislocation density. The motion of dislocations, in turn, heats the surroundings of the void due to plastic activity, producing a significant increase in local temperature. GNDs can be used to estimate the total dislocation length around a growing void by assuming that a certain number of dislocation shear loops are initially nucleated on the void surface and that they transport matter away from it [64–66]. This mechanism was proposed and analytically demonstrated by Lubarda et al. [67]; later MD simulations quantified the emission of dislocation shear loops and their eventual transformation into prismatic loops by a "lasso" mechanism for BCC crystals [68,69]. In the analysis presented below only the shear loop emission is evaluated because it is assumed that prismatic loops do not form under uniaxial compression [70],
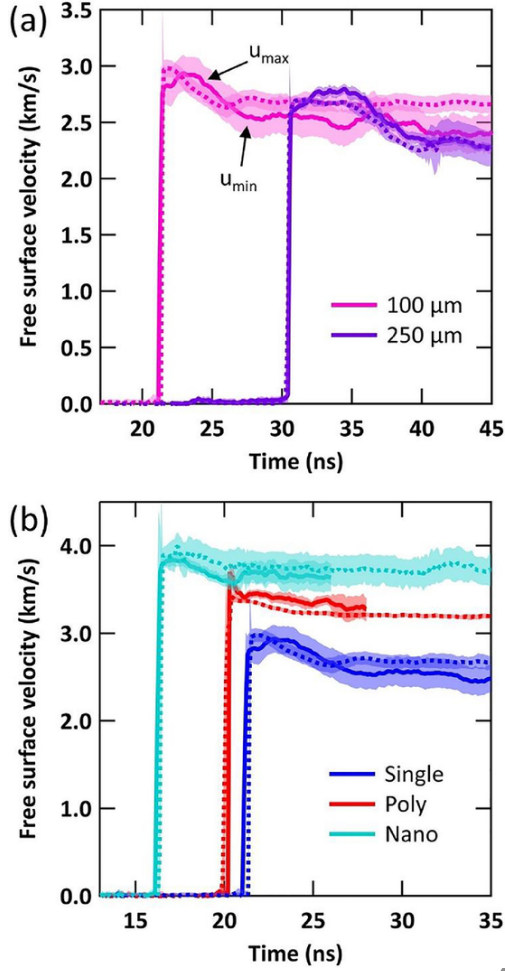
Figure 9. Representative VISAR traces (solid and dashed lines represent two channels of VISAR). (a) Strain-rate dependence in single crystal samples and (b) grain size dependence for samples of 100 μm thickness. Zero time represents start of drive laser and shaded region represents combined error from standard deviation and a systematic error.

until later when plastic flow reduces the background shear stress and the voids grow under greater stress triaxiality [71]. For the BCC structure, eight loops that propagate along BCC slip planes ($\{110\}/\langle\bar{1}11\rangle$) are initially assumed, and other sets of loops are also created as the void growth proceeds. Figure 14 depicts the growth of a void by the emission of various dislocations.

For every emission i of loops, the total length is,

$$\Delta L_t^i = 8\left(2\,L_1^i + L_2^i\right) \tag{4}$$

where L_1 and L_2 are the lengths of the screw and edge components, respectively. It is assumed that each loop expands to a distance of about 5-10 times the initial void radius. This is a reasonable assumption consistent with continuum plasticity treatments of void growth under hydrostatic tensile stresses. Once the loop reaches such distance, the applied shear stresses are sufficiently relaxed and the applied strain is accommodated by the emission of a new loop set. The total dislocation length around the void is:

$$L_{total}^i = L_{total}^{i-1} + \Delta L_t^i \tag{5}$$

The formation of the dislocation loops can be assumed to expand the void by an incremental volume dV [70] such that for

every emission i, the incremental and new void volumes are:

$$\Delta V^i \cong 2\sqrt{2}\pi r_{(i-1)}^2 b \tag{6}$$

$$V^i = V^{i-1} + \Delta V^i \tag{7}$$

Assuming spherical voids, the radius at the i'th emission event is:

$$r_i = \sqrt[3]{\left(\frac{3}{4\pi}\right)V^i} \tag{8}$$

The strain is computed assuming the increase in volume due to void growth is accommodated by an increase in the vertical dimension, a_3, in the unit cell:

$$V_{sample}^i = V_{sample}^{i-1} + \Delta V^i = a_1 a_2 a_3^i \tag{9}$$

where a_1 and a_2 remain constant during uniaxial tension and a_3 increases as:

$$a_3^i = \frac{V_{sample}^i}{a_1 a_2} \tag{10}$$

The corresponding strain increment dϵ and total strain are:

$$\Delta\epsilon^i = \frac{a_3^i - a_3^{i-1}}{a_3^{i-1}} \tag{11}$$

$$\epsilon^i = \Delta\,\epsilon^i + \epsilon^{i-1} \tag{12}$$

The results for each generated emission event can be found in Table 2 for an example case. They show that after ten dislocation emissions, the void radius is doubled, for an initial void radius of 1.5 nm. The work-hardened volume is considered as the volume limited by the spherical volumes corresponding to the work hardened radius $R = 10r_i$ and void radius r_i:

$$V_{wh}^i = \frac{4}{3}\pi\left(R^3 - r_i^3\right) \tag{13}$$

Dislocation density, ρ_{GND}^i, can then be calculated as the ratio between total dislocation length (Eq. 5) and work hardened volume (Eq. 13):

$$\rho_{GND}^i = \frac{L_{total}^i}{V_{wh}^i} \tag{14}$$

It is important to note that to accommodate for the increasing strain, the analytical model uses successive loop generation events, and that beyond 10% strain the dislocation configuration becomes too complex for the simple assumptions. The dislocation velocity (in m/s) as a function of shear stress, $\bar{v}(\tau)$, can be computed assuming a power law fit to the experimental results of Urabe and Weertman [72]:

$$\bar{v}(\tau) = 0.882\tau^{0.986} \tag{15}$$

The shear stresses were computed from our MD simulations of shock compression as [73]:

$$\tau = \frac{1}{2}\left[\sigma_{zz} - \frac{1}{2}\left(\sigma_{xx} + \sigma_{yy}\right)\right] \tag{16}$$

where σ_{xx}, σ_{yy}, and σ_{zz} are the hydrostatic stresses in the x, y, and z geometrical directions. The shear stresses obtained during the void nucleation and growth process and within that region are, on average, 600 MPa (0.6 GPa), giving an average dislocation velocity of approximately 500 m/s. Similar dislocation velocities were observed in our MD simulations of a single void
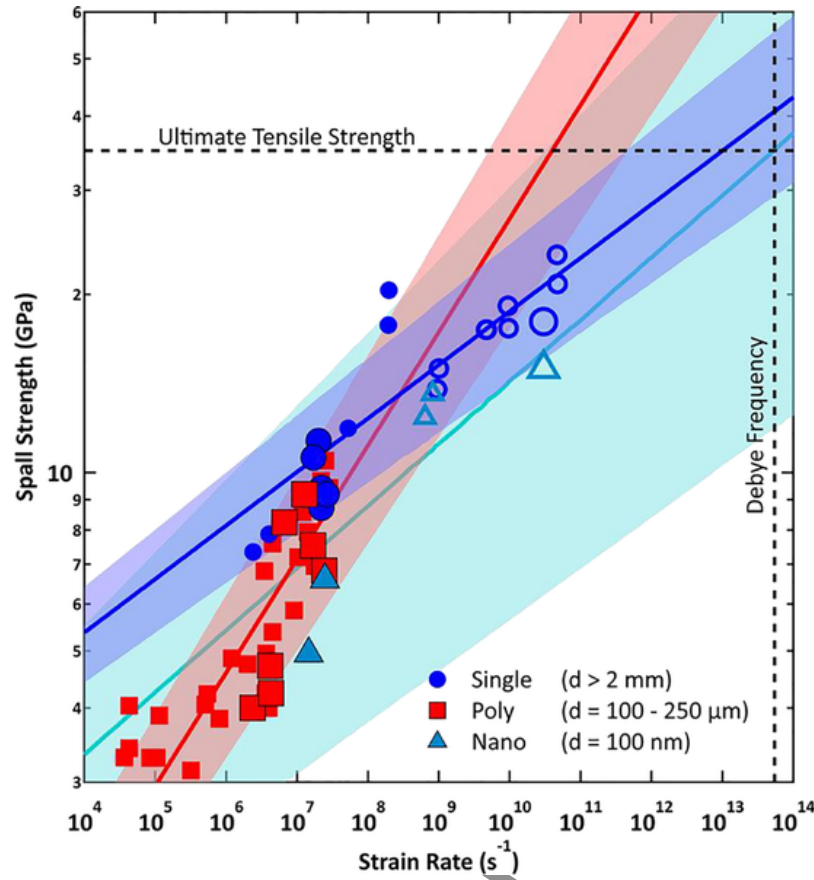
Figure 10. Spall strength versus strain rate on log-log scale with grain sizes from current experiments listed. Large symbols represent the current work, small symbols represent literature data, closed symbols represent experimental results, and open symbols represent simulation results. Power law fits to single crystal and nanocrystalline data converge near the ultimate tensile strength at ultra-high strain rate. Shaded regions represent 95% confidence intervals. References as follows: [9–11,13,15–18,33,57]. Reference [11] and [17] report grain size of 19-40 μm and 5 μm, respectively. All other references do not report grain size.

under high strain rate uniaxial tension and are also consistent with previous studies on BCC Ta under high strain rate uniaxial compression [69]. The plastic shear strain rate can be related to the mobile dislocation density ρ_m using Orowan's equation [74]:

$$\dot{e}_p = b\,\rho_m \bar{v}(\tau) \tag{17}$$

where b is the Burgers vector, approximately 0.27 nm for α iron. The mobile dislocation density ρ_m is a fraction of the total dislocation density, ρ_{GND}: $\rho_m = f \cdot \rho_{GND}$. f is a parameter that is assumed to gradually decrease with strain due to shear loops nucleating, propagating, and populating the work-hardened volume. This fraction takes the unity value as the first generation of loops leave the surface, and linearly decreases to 0.1 as the last emission of dislocations takes place due to two main factors: (1) dislocation loops consist of edge dislocation components that slip with high mobility, while screw components have limited mobility and (2) the rapid formation of junctions leads to a decrease in mobile dislocations with respect to the total number of dislocations [70].

Assuming adiabaticity, the temperature increase associated with plastic deformation is expressed as:

$$\frac{dT}{dt} = \frac{\beta}{\gamma \cdot C} \cdot \tau \cdot \dot{e}_P \tag{18}$$

where γ is the material density, C is the specific heat capacity, τ is the time-dependent shear stress, and β is the Quinney-Taylor parameter that represents the fraction of rate of

plastic work dissipated as heat [75], taken as equal to 1 for the sake of simplicity.

In reality, the evolution of dislocation density with plastic deformation is the result of the combined effects of dislocation generation and annihilation, with characteristic rates $\dot{\rho}_{gen}$ and $\dot{\rho}_{ann}$, respectively [76]:

$$\dot{\rho} = \dot{\rho}_{gen} - \dot{\rho}_{ann} \tag{19}$$

At the initial stages of plasticity, the material can be considered as pristine, and dislocations can expand and populate the surrounding volume freely. As the successive emission of loops takes place, the newly nucleated dislocations now propagate within a volume that contains dislocations. As more and more loops are emitted from the void surface, the plastic volume in the vicinity of the void has an increasing dislocation density and the dislocation forest requires a reduction of the mean free path. In consequence, annihilation events become more probable, to the limit that the annihilation rate becomes equal to the generation rate once the dislocation density reaches a critical value. Here, the saturation is around 10^{17} m^{-2}, consistent with conditions of shock compression in BCC metals [45,77]. As a first approximation, the dislocation annihilation rate is considered to be proportional to the dislocation density and inversely proportional to the mean free path before they encounter dislocations of opposite sign [78]. Indeed, the Kocks-Mecking theory has different power dependencies for the two terms, $\dot{\rho}_{gen}$ and $\dot{\rho}_{ann}$ [79] and a detailed treatment
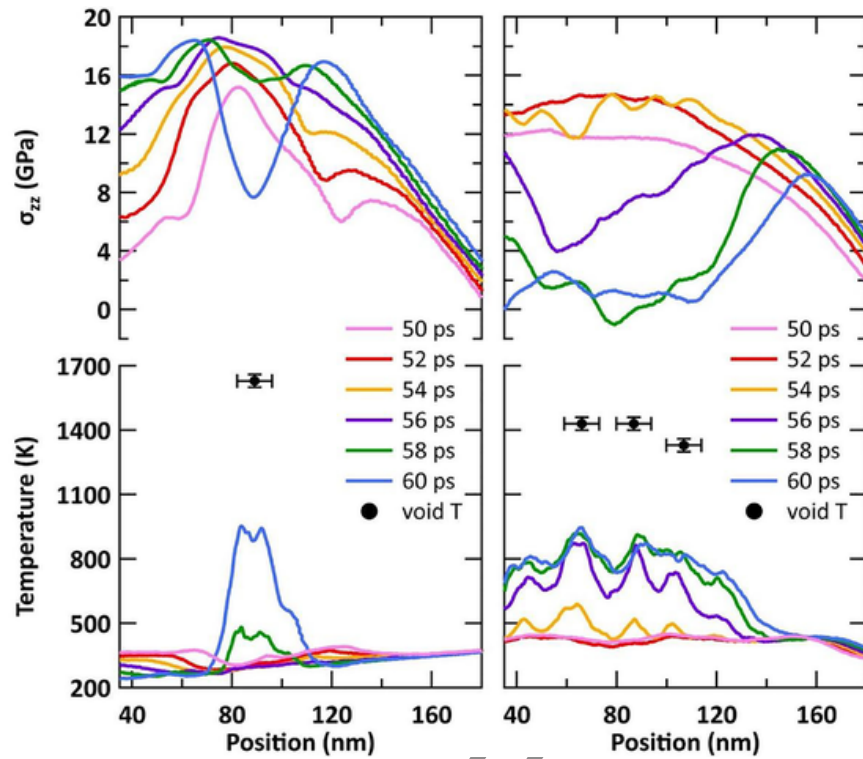
Figure 11. MD calculations of pressure in the z-direction (parallel to loading) and temperature in the single crystal (left) and nanocrystal (right) with 10 nm average grain size. Void T symbols correspond to the peak temperature in voids at 60 ns. Initial shock direction goes from left to right.
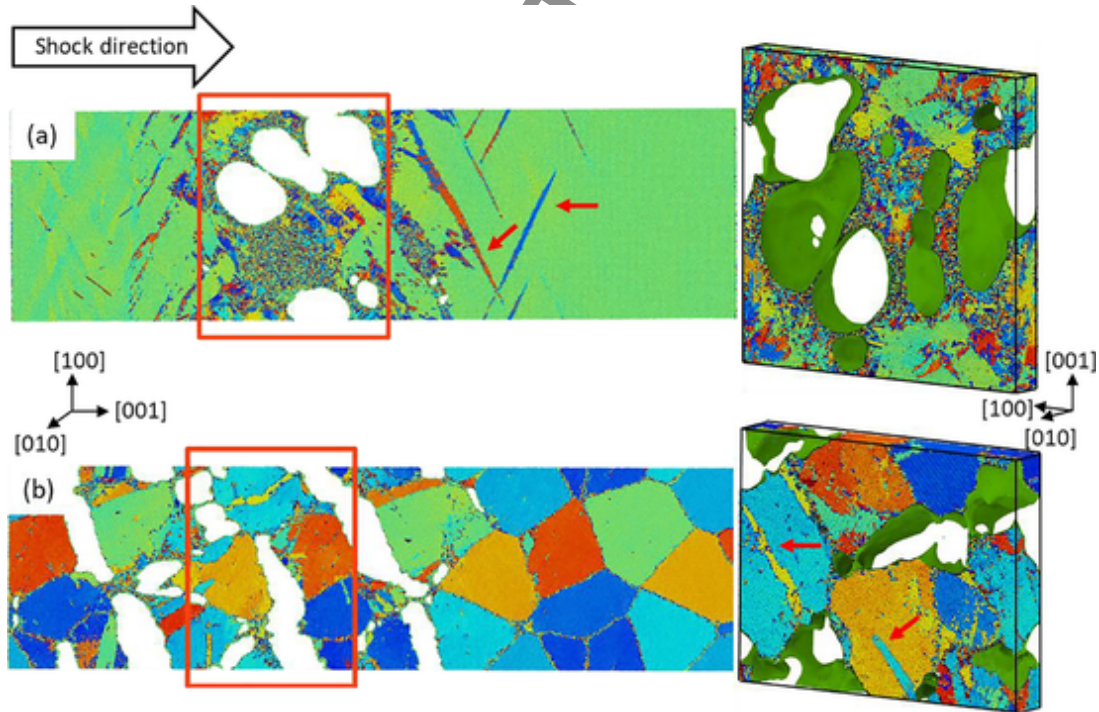

Figure 12. MD simulation of shocked (a) single crystal and (b) nanocrystal iron (10 nm grain size) at 68 ps with enlarged view of the spalling region. Atom coloring is based on the relative crystalline orientation and white corresponds to void region. Enlarged views (right) are rotated to highlight void where green surfaces correspond to spall surface. Initial shock direction goes from left to right. Arrows point to twin boundaries.

of the exact functional form for these high strain-rate conditions is beyond the scope of this work.

Estimations of the analytical model are presented in Fig. 15. It is reasonable that, when dislocation activity starts, the total and mobile dislocation densities are similar, but the

rapid formation of junctions leads to a decrease in mobile dislocations with respect to the total number of dislocations. As the mobile dislocation density reaches the saturation value ($\sim 10^{17}$ m^{-2}), the $\dot{\rho}_{gen}$ and $\dot{\rho}_{ann}$ can be considered to be equal, such that $\dot{\rho}$ becomes zero. Thus, the total dislocation density,
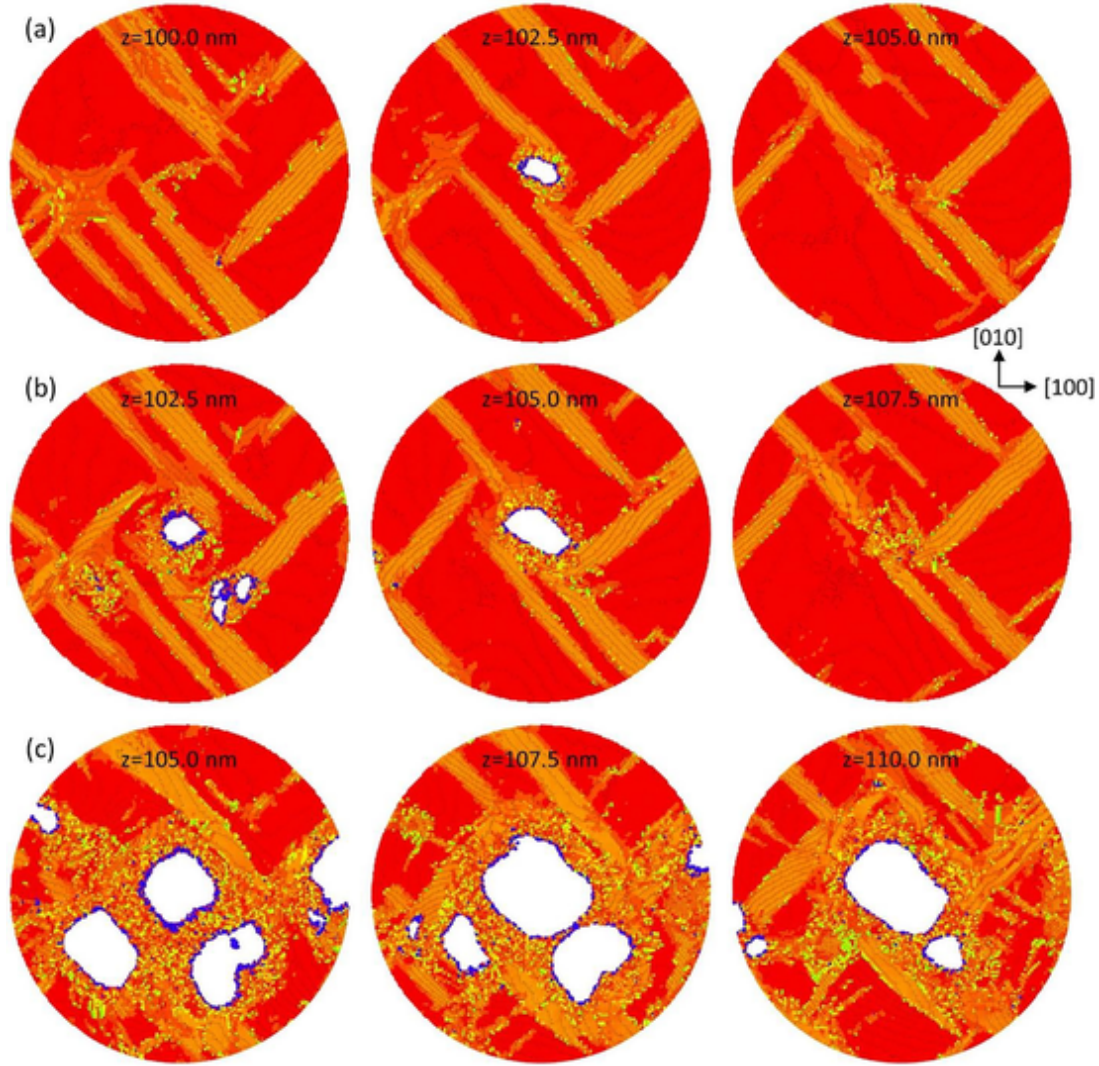
Figure 13. Slices of the single crystal sample along the shock direction at (a) 56 ps, (b) 58 ps, and (c) 62 ps. Coloring corresponds to local orientation of the atoms. Red corresponds to [100]-oriented BCC structure and orange are {110} oriented domains, which correspond to twins. Their interaction leads to the formation of one (top row) or more voids (mid row) of spheroidal shape. The bottom row shows that, at a later stage, the voids have grown and are closer to each other, leading to coalescence. The strong changes in color in the surrounding of the voids point to massive disorder, typically associated with melting.

considering both generation and annihilation events, remains constant at the saturation point. The density of mobile dislocation decreases beyond a strain of 0.09.

The comparison of analytical and MD predictions is revealing. The MD-predicted dislocation density rises rapidly with plastic strain up to 5×10^{16} m^{-2} and then increases at a much lower rate. Although there are differences between the two predictions, the results are fairly consistent. Additionally, the GND density estimated from recovered samples (10^{15} m^{-2}) is within one order of magnitude from MD simulations and analytical predictions – a reasonable difference given the assumptions of the model and the underestimation of the EBSD GND technique.

The emission and propagation of dislocations for ten successive generation events increases the temperature to 590 K, an increase of over 250 K above the initial value. This corresponds to an increase in void radius from 1.5 to 3 nm. GND-predictions can also be compared with the temperature profiles of the spall simulations (Fig. 11). The temperature rise at void initiation at 58 ps and 54-56 ps in single and nanocrystal iron, respectively, is similarly ~250 K. The void nucleation in the spall simulations exhibits important differences not in-

cluded in the model; e.g. under spall conditions, voids nucleate at twin-twin intersections in a heavily stressed environment, under high strain rate conditions, whereas the model presented in this section contains a pre-existing void under equilibrium conditions. Several other factors may also play a role under shock loading conditions, such as phase transformations, microstructural evolution, thermal softening, heat conduction or even electron-phonon coupling [80,81]. In particular, heat conduction can play an important role in void growth as pointed out by Wu et al. [81] since, depending on the efficiency of the heat conduction, voids grow either adiabatically or isothermally, in the limiting cases. One possibility or the other depends mainly on the initial void size, void growth rate, and material properties such as thermal conductivity, mass density, specific heat and yield strain. According to Wu et al. [81], the criterion to determine when the adiabatic void growth or the isothermal void growth idealizations should be considered is:

$$\begin{cases} \frac{a\,\dot{a}}{\Omega} < 0.01, \ for \ isothermal \ growth \\ \frac{a\,\dot{a}}{\Omega} > 100, \ for \ adiabatic \ growth \end{cases} \tag{20}$$
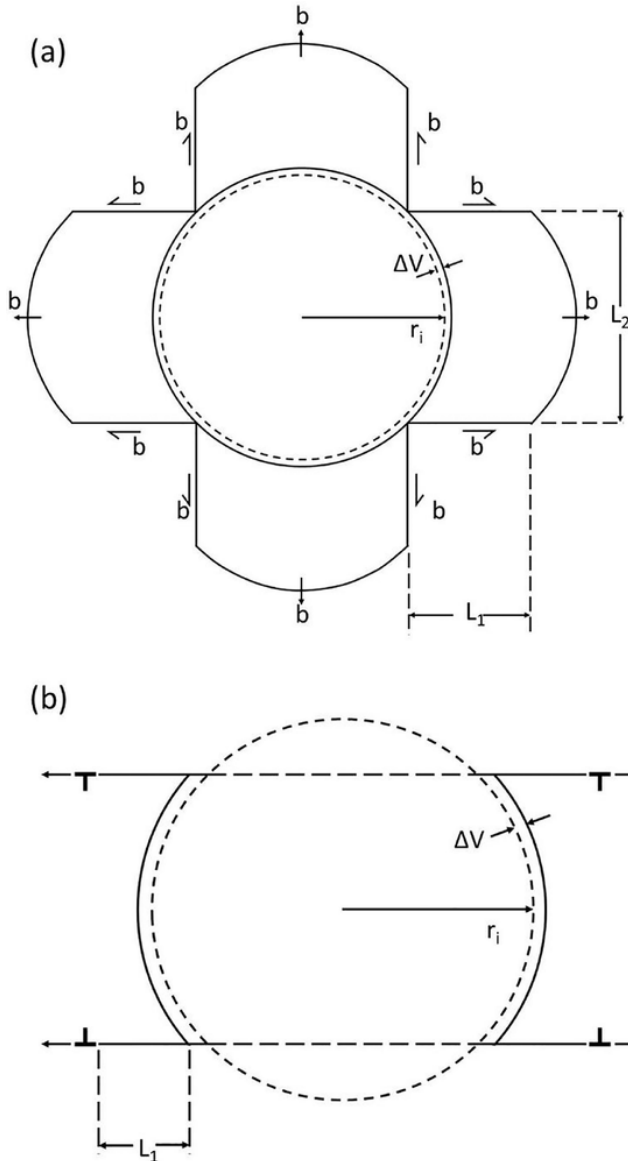
Figure 14. Schematic representation of void growth process via GND emission from (a) top and (b) side view. Initial void of radius r_i grows by ΔV after emission of several dislocations of Burgers vector, b.

where a is the initial void radius, $\dot{a}$ is the void growth rate, and $\Omega = 2.6k/\rho c_p \varepsilon_\gamma^{2/3}$, where k is the thermal conductivity, ρ is the mass density, c_p the specific heat capacity and ε_y the yield strain. This opens the possibility for improvements of the current model by introducing modifications to Eq. 18, that would result from incorporating a heat conduction term into the energy balance equation. At later stages of void growth during spall, however, voids grow much more rapidly, justifying a treatment using an adiabatic approximation [81].

Although the simplified analytical model presented here may not capture other effects stated above and that may play a role in void nucleation and growth, the 250 K temperature increase is similar to what is seen in MD. The incorporation of more complex dislocation phenomena and this promising result may pave the ground for future developments of such models.

4. Conclusions

The effect of initial nano/microstructure on the spall behavior of iron at 10^6 s^{-1} – 10^7 s^{-1} strain rate was experimentally investigated in thin foils shocked by a 100 J 2ω laser producing a triangular shock wave (P ~60 GPa) in the material and spallation at the rear free surface. This study of spall in iron provides insight into the complex dynamic failure process. The following are the main findings of these systematic experiments coupled with analytical calculations and MD simulations:

• A novel soft recovery technique was used in conjunction with VISAR to obtain high quality microstructural and velocity data for every shot.
• Single crystal samples exhibit a characteristic dimpled spall surface that is indicative of ductile failure known to occur after the reversible α-ε phase transition [18]. This is the result of nano-sized voids that nucleate, grow, and coalesce, causing failure. Smaller grained poly- and nanocrystalline iron have a blistered or streaked spall surface due to failure along grain boundaries, in addition to minor dimpling. Grain boundaries are known to be preferential void nucleation sites, and are ultimately the cause of failure. Therefore, the spall strength of single crystal iron is higher than that of poly- and nanocrystalline iron at strain rates tested owing to the larger number of grain boundaries that weaken the material in the latter cases. This "reverse" Hall-Petch relationship is also seen in many other spalled materials, both BCC and FCC [7,8,63,82–84], and is due to the greater strain-rate sensitivity of plastic flow in comparison with grain-boundary cohesion. Experimental results from this study
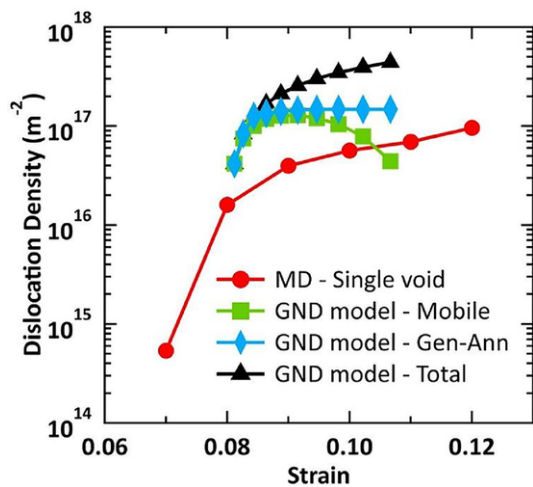
Table 2
Estimation of temperature increase by GND emission.

Emission no.	ΔV (nm^3)	V_i (nm^3)	r_i (nm)	V_{wh} (nm^3)	L_{total} (nm)	ρ_{mobile} (10^{16} m^{-2})	ρ_{gnd} (10^{16} m^{-2})	T (K)
0	0	14.13	1.5	0	0	0	0	300
1	4.94	19.07	1.66	4169.72	173.33	4.16	4.16	314.02
2	6.03	25.10	1.82	4163.69	348.06	7.52	8.34	338.82
3	7.24	32.34	1.98	4156.45	524.19	10.1	12.6	371.68
4	8.57	40.91	2.14	4147.88	701.76	11.8	16.9	409.38
5	10.03	50.94	2.30	4137.85	880.75	12.8	21.3	449.22
6	11.61	62.54	2.46	4126.24	1061.18	12.9	25.7	488.51
7	13.31	75.85	2.63	4112.93	1243.06	12.1	30.2	524.67
8	15.13	90.99	2.79	4097.80	1426.40	10.4	34.8	555.22
9	17.09	108.07	2.95	4080.71	1611.19	7.90	39.5	577.81
10	19.16	127.24	3.12	4061.55	1797.45	4.43	44.3	590.18

Parameters for Eqs. 4 through 19 are taken as follows: R = 10 nm, γ = 7300 kg/m3, C = 460 J/(kg K), τ = 0.6 GPa after MD simulations, $\bar{v}$ = 500 m/s [72].

Figure 15. Comparison of model predictions of dislocation density with a MD simulation of iron single crystal with a void. When considering only generation events, the dislocation density increases with strain (red). If annihilation events are included (blue), the saturation density of 10^{17} m^{-2} must be taken into account. The total dislocation density (black), includes density of mobile dislocations (green).

provide the necessary evidence that the reverse phase transformation has occurred: a ductile spall surface is observed, and peak pressures reached well above the α to ε phase transition pressure.

- MD simulations show that in single crystal iron, the interaction of twin boundaries becomes a preferential site for void nucleation. Further void growth results in a local highly disordered structure that increases the temperature to near-melting conditions around voids. As more voids nucleate and grow, they coalesce, leading to the formation of a spallation plane. The large volume density of grain boundaries in nanocrystalline simulations facilitates void nucleation sites and leads to preferential failure along boundaries that are perpendicular to the shock direction. Failure in single crystal iron appears to be more localized, while in nanocrystal iron it is more distributed and leads to a lower spall strength. Despite differences in strain rates, the simulated spall strengths follow the same trend as experimental results.

- An analytical model was developed which predicts a dislocation density that is consistent with MD simulations and saturates at approximately 10^{17} m^{-2}. This simplified model uses nanometer sized voids as nucleation sites for geometrically necessary dislocations. As void growth proceeds, more dislocation loops are created and heat the surroundings as they propagate. It is assumed that the evolution of dislocation density is a combination of dislocation generation and annihilation rates.

- Both MD simulations and analytical calculations predict significant temperature rises which can, at peak, lead to melting of the void surfaces. They explain the apparent melting behavior observed in postshock characterization.

- Experimental results, MD simulations, and analytical modelling predict density of geometrically necessary dislocations to be $10^{15} - 10^{17}$ m^{-2}. This is a reasonable range of values considering the assumptions made in the analytical model and the underestimation of GND density from the EBSD maps. Additionally, EBSD maps of dislocation density support simulation findings of circular void growth in single crystal iron and intragranular plasticity in polycrystalline iron.

Supplementary materials

Supplementary material associated with this article can be found, in the online version, at doi:10.1016/j.actamat.2021.117072.

References

[1] T.H. Judge, P.J. Buttkus, Ballistic and Spall Tests for Aircrew Body Armor (1972) 74.

[2] H.J. Melosh, Impact Ejection, Spallation, and the Origin of Meteorites (1984) 27.

[3] NASA, Meteroroid Damage Assessment, Space Veh. Des. Criteria. (1970).

[4] M.A. Meyers, Dynamic Behavior of Materials, John Wiley & Sons, 1994.

[5] T. Antoun (Ed.), Spall fracture, Springer, New York, 2003.

[6] S.V. Razorenov, Large Tensions and Strength of Iron in Different Structure States, in: AIP Conf. Proc., AIP, Baltimore, Maryland (USA), 2006: pp. 650–653. https://doi.org/10.1063/1.2263406.

[7] T.P. Remington, E.N. Hahn, S. Zhao, R. Flanagan, J.C.E. Mertens, S. Sabbaghianrad, T.G. Langdon, C.E. Wehrenberg, B.R. Maddox, D.C. Swift, B.A. Remington, N. Chawla, M.A. Meyers, Spall strength dependence on grain size and strain rate in tantalum, Acta Mater 158 (2018) 313–329, doi:10.1016/j.actamat.2018.07.048.

[8] H. Jarmakani, B. Maddox, C.T. Wei, D. Kalantar, M.A. Meyers, Laser shock-induced spalling and fragmentation in vanadium, Acta Mater 58 (2010) 4604–4628, doi:10.1016/j.actamat.2010.04.027.

[9] H. Shu, X. Huang, H. Pan, J. Ye, F. Zhang, G. Jia, Z. Fang, Y. Tu, Z. Xie, S. Fu, Plastic behavior of steel and iron in high strain rate regime, Int. J. Fract. 206 (2017) 81–93, doi:10.1007/s10704-017-0202-6.

[10] G.V. Garkushin, N.S. Naumova, S.A. Atroshenko, S.V. Razorenov, Influence of the reversible α–ε phase transition and preliminary shock compression on the spall strength of armco iron, Tech. Phys. 61 (2016) 84–90, doi:10.1134/S1063784216010102.

[11] E.B. Zaretsky, G.I. Kanel, Yield stress, polymorphic transformation, and spall fracture of shock-loaded iron in various structural states and at various temperatures, J. Appl. Phys. 117 (2015) 195901, doi:10.1063/1.4921356.

[12] C. Voltz, Study of Spalling for High Purity Iron below and above Shock Induced α ⇔ ε Phase Transition, in: AIP Conf. Proc., AIP, Portland, Oregon (USA), 2004: pp. 511–516. https://doi.org/10.1063/1.1780289.

[13] A.E. Mayer, Dynamic shear and tensile strength of iron: Continual and atomistic simulation, Mech. Solids. 49 (2014) 649–656, doi:10.3103/S0025654414060065.

[14] N. Gunkelmann, E.M. Bringa, H.M. Urbassek, Influence of phase transition on shock-induced spallation in nanocrystalline iron, J. Appl. Phys. 118 (2015) 185902, doi:10.1063/1.4935452.

[15] S.I. Ashitkov, V.V. Zhakhovsky, N.A. Inogamov, P.S. Komarov, M.B. Agranat, G.I. Kanel, *The behavior of iron under ultrafast shock loading driven by a femtosecond laser*, in: Tampa Bay, Florida, USA, 2017: p. 100035. https://doi.org/10.1063/1.4971660.

[16] S.I. Ashitkov, P.S. Komarov, M.B. Agranat, G.I. Kanel, V.E. Fortov, Achievement of ultimate values of the bulk and shear strengths of iron irradiated by femtosecond laser pulses, JETP Lett 98 (2013) 384–388, doi:10.1134/S0021364013200022.

[17] J. Wang, R.F. Smith, J.H. Eggert, D.G. Braun, T.R. Boehly, J.Reed Patterson, P.M. Celliers, R. Jeanloz, G.W. Collins, T.S. Duffy, Ramp compression of iron to 273 GPa, J. Appl. Phys. 114 (2013) 023513, doi:10.1063/1.4813091.

[18] T. de Rességuier, M. Hallouin, Effects of the $\alpha - \varepsilon$ phase transition on wave propagation and spallation in laser shock-loaded iron, Phys. Rev. B. 77 (2008) 174107, doi:10.1103/PhysRevB.77.174107.

[19] D. Bancroft, E.L. Peterson, S. Minshall, Polymorphism of Iron at High Pressure, J. Appl. Phys. 27 (1956) 291–298, doi:10.1063/1.1722359.

[20] Anna K. Zurek, M.A. Meyers, Microstructural aspects of dynamic failure, in: High-Press. Shock Compression Solids II, Springer, New York, NY, 1996, pp. 25–70.

[21] J.O. Erkman, Smooth Spalls and the Polymorphism of Iron, J. Appl. Phys. 32 (1961) 939–944, doi:10.1063/1.1736137.

[22] L.M. Barker, R.E. Hollenbach, Shock wave study of the $\alpha \rightleftarrows \varepsilon$ phase transition in iron, J. Appl. Phys. 45 (1974) 4872–4887, doi:10.1063/1.1663148.

[23] L.M. Barker, R.E. Hollenbach, Laser interferometer for measuring high velocities of any reflecting surface, J. Appl. Phys. 43 (1972) 4669–4675, doi:10.1063/1.1660986.

[24] P.M. Celliers, D.K. Bradley, G.W. Collins, D.G. Hicks, T.R. Boehly, W.J. Armstrong, Line-imaging velocimeter for shock diagnostics at the OMEGA laser facility, Rev. Sci. Instrum. 75 (2004) 4916–4929, doi:10.1063/1.1807008.

[25] Inertial Confinement Fusion quarterly report, 5, Lawrence Livermore National Lab., CA (United States), 1995 April–June 1995, doi:10.2172/187252.

[26] E.N. Hahn, T.C. Germann, R.J. Ravelo, J.E. Hammerberg, M.A. Meyers, *Non-equilibrium molecular dynamics simulations of spall in single crystal tantalum*, in: Tampa Bay, Florida, USA, 2017: p. 070006. https://doi.org/10.1063/1.4971594.

[27] E.N. Hahn, T.C. Germann, R. Ravelo, J.E. Hammerberg, M.A. Meyers, On the ultimate tensile strength of tantalum, Acta Mater 126 (2017) 313–328, doi:10.1016/j.actamat.2016.12.033.

[28] N. Amadou, T. de Resseguier, A. Dragon, E. Brambrink, Coupling between plasticity and phase transition in shock- and ramp-compressed single-crystal iron, Phys. Rev. B. 98 (2018) 024104, doi:10.1103/PhysRevB.98.024104.

[29] N. Gunkelmann, E.M. Bringa, D.R. Tramontina, C.J. Ruestes, M.J. Suggit, A. Higginbotham, J.S. Wark, H.M. Urbassek, Shock waves in polycrystalline iron: Plasticity and phase transitions, Phys. Rev. B. 89 (2014) 140102, doi:10.1103/PhysRevB.89.140102.

[30] N. Amadou, T.D. Resseguier, A. Dragon, E. Brambrink, Effects of orientation, lattice defects and temperature on plasticity and phase transition in ramp-compressed single crystal iron, Comput. Mater. Sci. 172 (2020) 109318, doi:10.1016/j.commatsci.2019.109318.

[31] B.L. Holian, Plasticity Induced by Shock Waves in Nonequilibrium Molecular-Dynamics Simulations, Science 280 (1998) 2085–2088, doi:10.1126/science.280.5372.2085.

[32] P. Hirel, Atomsk: A tool for manipulating and converting atomic data files, Comput. Phys. Commun. 197 (2015) 212–219, doi:10.1016/j.cpc.2015.07.012.

[33] N. Gunkelmann, D.R. Tramontina, E.M. Bringa, H.M. Urbassek, Morphological changes in polycrystalline Fe after compression and release, J. Appl. Phys. 117 (2015) 085901, doi:10.1063/1.4913622.

[34] N. Gunkelmann, Interplay of plasticity and phase transformation in shock wave propagation in nanocrystalline iron, New J Phys (2014) 13.

[35] H.-T. Luu, R.G.A. Veiga, N. Gunkelmann, Atomistic Study of the Role of Defects on $\alpha \rightarrow \epsilon$ Phase Transformations in Iron under Hydrostatic Compression, Metals 9 (2019) 1040, doi:10.3390/met9101040.

[36] N. Gunkelmann, E.M. Bringa, K. Kang, G.J. Ackland, C.J. Ruestes, H.M. Urbassek, Polycrystalline iron under compression: Plasticity and phase transitions, Phys. Rev. B. 86 (2012) 144111, doi:10.1103/PhysRevB.86.144111.

[37] S. Plimpton, *Fast Parallel Algorithms for Short- Range Molecular Dynamics*, (n.d.) 44.

[38] A. Stukowski, Visualization and analysis of atomistic simulation data with OVITO–the Open Visualization Tool, Model. Simul. Mater. Sci. Eng. 18 (2010) 015012, doi:10.1088/0965-0393/18/1/015012.

[39] A. Stukowski, Structure identification methods for atomistic simulations of crystalline materials, Model. Simul. Mater. Sci. Eng. 20 (2012) 045021, doi:10.1088/0965-0393/20/4/045021.

[40] P.M. Larsen, S. Schmidt, J. Schiotz, Robust structural identification via polyhedral template matching, Model. Simul. Mater. Sci. Eng. 24 (2016) 055007, doi:10.1088/0965-0393/24/5/055007.

[41] A. Stukowski, Computational Analysis Methods in Atomistic Modeling of Crystals, JOM 66 (2014) 399–407, doi:10.1007/s11837-013-0827-5.

[42] A. Stukowski, K. Albe, Extracting dislocations and non-dislocation crystal defects from atomistic simulation data, Model. Simul. Mater. Sci. Eng. 18 (2010) 085001, doi:10.1088/0965-0393/18/8/085001.

[43] W. Cai, W.D. Nix, Materials Research Society, Imperfections in crystalline solids, 2016.

[44] W. Pantleon, Resolving the geometrically necessary dislocation content by conventional electron backscattering diffraction, Scr. Mater. 58 (2008) 994–997, doi:10.1016/j.scriptamat.2008.01.050.

[45] C.H. Lu, B.A. Remington, B.R. Maddox, B. Kad, H.S. Park, S.T. Prisbrey, M.A. Meyers, Laser compression of monocrystalline tantalum, Acta Mater 60 (2012) 6601–6620, doi:10.1016/j.actamat.2012.08.026.

[46] C.H. Lu, B.A. Remington, B.R. Maddox, B. Kad, H.S. Park, M. Kawasaki, T.G. Langdon, M.A. Meyers, Laser compression of nanocrystalline tantalum, Acta Mater 61 (2013) 7767–7780, doi:10.1016/j.actamat.2013.09.016.

[47] D.E. Grady, The spall strength of condensed matter, J. Mech. Phys. Solids. 36 (1988) 353–384, doi:10.1016/0022-5096(88)90015-4.

[48] M.A. Meyers, C.Taylor Aimone, Dynamic fracture (spalling) of metals, Prog. Mater. Sci. 28 (1983) 1–96, doi:10.1016/0079-6425(83)90003-8.

[49] G. Avramovic-Cingara, Ch.A.R. Saleh, M.K. Jain, D.S. Wilkinson, Void Nucleation and Growth in Dual-Phase Steel 600 during Uniaxial Tensile Testing, Metall. Mater. Trans. A. 40 (2009) 3117–3127, doi:10.1007/s11661-009-0030-z.

[50] Y. Fan, A. Kushima, S. Yip, B. Yildiz, Mechanism of Void Nucleation and Growth in bcc Fe: Atomistic Simulations at Experimental Time Scales, Phys. Rev. Lett. 106 (2011) 125501.

[51] B. Margolin, G. Karzov, V. Shvetsova, V. Kostylev, Modelling for Trancrystalline and Intercrystalline Fracture by Void Nucleation and Growth, Fatigue Fract. Eng. Mater. Struct. 21 (1998) 123–137, doi:10.1046/j.1460-2695.1998.00474.x.

[52] R.E. Rudd, Void growth in bcc metals simulated with molecular dynamics using the Finnis–Sinclair potential, Philos. Mag. 89 (2009) 3133–3161, doi:10.1080/14786430903222529.

[53] E.T. Seppala, J.F. Belak, R.E. Rudd, Effect of stress triaxiality on void growth in dynamic fracture of metals: A molecular dynamics study, Phys. Rev. B. 69 (2004) 134101.

[54] K. Jagannadham, H.G.F. Wilsdorf, Low energy dislocation structures associated with cracks in ductile fracture, Mater. Sci. Eng. 81 (1986) 273–292, doi:10.1016/0025-5416(86)90268-5.

[55] P. Noell, J. Carroll, K. Hattar, B. Clark, B. Boyce, Do voids nucleate at grain boundaries during ductile rupture?, Acta Mater 137 (2017) 103–114, doi:10.1016/j.actamat.2017.07.004.

[56] D. Curran, Dynamic failure of solids, Phys. Rep. 147 (1987) 253–388, doi:10.1016/0370-1573(87)90049-4.

[57] S.V. Razorenov, G.I. Kanel, V.E. Fortov, Iron at high negative pressures, J. Exp. Theor. Phys. Lett. 80 (2004) 348–350, doi:10.1134/1.1825120.

[58] E.N. Hahn, S.J. Fensin, T.C. Germann, *The role of grain boundary orientation on void nucleation in tantalum*, in: St. Louis, MO, USA, 2018: p. 050008. https://doi.org/10.1063/1.5044791.

[59] J.P. Escobedo, E.K. Cerreta, D. Dennis-Koller, Effect of Crystalline Structure on Intergranular Failure During Shock Loading, JOM 66 (2014) 156–164, doi:10.1007/s11837-013-0798-6.

[60] M. Cheng, C. Li, M.X. Tang, L. Lu, Z. Li, S.N. Luo, Intragranular void formation in shock-spalled tantalum: Mechanisms and governing factors, Acta Mater 148 (2018) 38–48, doi:10.1016/j.actamat.2018.01.029.

[61] A.G. Perez-Bergquist, E.K. Cerreta, C.P. Trujillo, F. Cao, G.T. Gray, Orientation dependence of void formation and substructure deformation in a spalled copper bicrystal, Scr. Mater. 65 (2011) 1069–1072, doi:10.1016/j.scriptamat.2011.09.015.

[62] Y. Deng, C. Deng, Size and rate dependent grain boundary motion mediated by disconnection nucleation, Acta Mater 131 (2017) 400–409, doi:10.1016/j.actamat.2017.04.018.

[63] G.I. Kanel, S.V. Razorenov, K. Baumung, J. Singer, Dynamic yield and tensile strength of aluminum single crystals at temperatures up to the melting point, J. Appl. Phys. 90 (2001) 136–143, doi:10.1063/1.1374478.

[64] M.F. Ashby, The deformation of plastically non-homogeneous materials, Philos. Mag. J. Theor. Exp. Appl. Phys. 21 (1970) 399–424, doi:10.1080/14786437008238426.

[65] M.F. Ashby, L. Johnson, On the generation of dislocations at misfitting particles in a ductile matrix, Philos. Mag. 20 (1969) 1009–1022, doi:10.1080/14786436908228069.

[66] M.F. Ashby, S.H. Gelles, L.E. Tanner, The stress at which dislocations are generated at a particle-matrix interface, Philos. Mag. 19 (1969) 757–771, doi:10.1080/14786436908216332.

[67] V.A. Lubarda, M.S. Schneider, D.H. Kalantar, B.A. Remington, M.A. Meyers, Void growth by dislocation emission, Acta Mater 52 (2004) 1397–1408, doi:10.1016/j.actamat.2003.11.022.

[68] T.P. Remington, C.J. Ruestes, E.M. Bringa, B.A. Remington, C.H. Lu, B. Kad, M.A. Meyers, Plastic deformation in nanoindentation of tantalum: A new mechanism for prismatic loop formation, Acta Mater 78 (2014) 378–393, doi:10.1016/j.actamat.2014.06.058.

[69] Y. Tang, E.M. Bringa, B.A. Remington, M.A. Meyers, Growth and collapse of nanovoids in tantalum monocrystals, Acta Mater 59 (2011) 1354–1372, doi:10.1016/j.actamat.2010.11.001.

[70] C.J. Ruestes, E.M. Bringa, A. Stukowski, J.F. Rodríguez Nieva, Y. Tang, M.A. Meyers, Plastic deformation of a porous bcc metal containing nanometer sized voids, Comput. Mater. Sci. 88 (2014) 92–102, doi:10.1016/j.commatsci.2014.02.047.

[71] R.E. Rudd, E.T. Seppälä, L.M. Dupuy, J. Belak, Void coalescence processes quantified through atomistic and multiscale simulation, J. Comput.-Aided Mater. Des. 14 (2007) 425–434, doi:10.1007/s10820-007-9054-0.

[72] N. Urabe, J. Weertman, Dislocation mobility in potassium and iron single crystals, Mater. Sci. Eng. 18 (1975) 41–49.

[73] Y.B. Zel'dovich, Y.P. Raizer, Physics of Shock Waves and High-Temperature Hydrodynamic Phenomena, Courier Corporation, 2002.

[74] E. Orowan, Problems of plastic gliding, Proc. Phys. Soc. 52 (1940) 8–22, doi:10.1088/0959-5309/52/1/303.

[75] H. Quinney, G.I. Taylor, The emission of the latent energy due to previous cold working when a metal is heated, Proc. R. Soc. Lond. Ser. - Math. Phys. Sci. 163 (1937) 157–181, doi:10.1098/rspa.1937.0217.

[76] Z. Li, S. Zhao, B. Wang, S. Cui, R. Chen, R.Z. Valiev, M.A. Meyers, The effects of ultra-fine-grained structure and cryogenic temperature on adiabatic shear localization in titanium, Acta Mater 181 (2019) 408–422, doi:10.1016/j.actamat.2019.09.011.

[77] S. Nemat-Nasser, J.B. Isaacs, M. Liu, Microstructure of High-Strain-Rate Deformed Tantalum, Acta Mater 46 (1998) 1307–1325.

[78] K.M. Davoudi, J.J. Vlassak, Dislocation evolution during plastic deformation: Equations vs. discrete dislocation dynamics study, J. Appl. Phys. 123 (2018) 085302, doi:10.1063/1.5013213.

[79] H. Mecking, U.F. Kocks, Kinetics of flow and strain-hardening, Acta Metall 29 (1981) 1865–1875, doi:10.1016/0001-6160(81)90112-7.

[80] D.C. Wallace, Nature of the process of overdriven shocks in metals, Phys. Rev. B. 24 (1981) 5607–5615, doi:10.1103/PhysRevB.24.5607.

[81] X.Y. Wu, K.T. Ramesh, T.W. Wright, The effects of thermal softening and heat conduction on the dynamic growth of voids, Int. J. Solids Struct. 40 (2003) 4461–4478, doi:10.1016/S0020-7683(03)00214-2.

[82] G.I. Kanel, S.V. Razorenov, A.V. Utkin, V.E. Fortov, K. Baumung, H.U. Karow, D. Rusch, V. Licht, Spall strength of molybdenum single crystals, J. Appl. Phys. 74 (1993) 7162–7165, doi:10.1063/1.355032.

[83] R.W. Minich, J.U. Cazamias, M. Kumar, A.J. Schwartz, Effect of microstructural length scales on spall behavior of copper, Metall. Mater. Trans. A. 35 (2004) 2663–2673, doi:10.1007/s11661-004-0212-7.

[84] D.A. Dalton, D.L. Worthington, P.A. Sherek, N.A. Pedrazas, H.J. Quevedo, A.C. Bernstein, P. Rambo, J. Schwarz, A. Edens, M. Geissel, I.C. Smith, E.M. Taleff, T. Ditmire, Microstructure dependence of dynamic fracture and yielding in aluminum and an aluminum alloy at strain rates of 2×10^6 s^{-1} and faster, J. Appl. Phys. 110 (2011) 103509, doi:10.1063/1.3660214.